Moment resisting splice of timber beams using long threaded rods and grout-filled couplers – Experimental results and predictive models

Martin Cepelka[1*], Kjell Arne Malo[1**]

[1] Department of Structural Engineering, Norwegian University of Science and Technology (NTNU), Rich. Birkelandsvei 1A, 7491, Trondheim, Norway

[*] corresponding author, martin.cepelka@ntnu.no , +4795409031

[**] kjell.malo@ntnu.no

Abstract

In order to achieve larger spans of timber arch bridges, glulam massive timber sections must be spliced on-site by moment resisting and rotationally stiff joints. In this paper, a novel timber splice connection utilizing long threaded rods and grout-filled couplers is presented. Flexural characteristics of the splice joint were investigated by full-scale experimental tests and 3D finite element models. An analytical model is proposed for determining the moment capacity and the rotational stiffness of the splice connection. The experimentally measured efficiency of the splice connection with regard to moment capacity and rotational stiffness was 69 % and 66 %, respectively.

Keywords: timber beam splice connection, long threaded rods, grout-filled couplers, experimental testing, 3D finite element model, rotational stiffness, moment capacity

1. Introduction

The development of glued laminated timber (glulam) allows for production of timber elements with nearly unlimited cross-sectional dimensions. However, production and transportation impose limitations on the length of timber elements. The maximum length of glulam elements is in a range of 30 to 40 m for straight elements, and approximately 20 to 30 m for curved elements in dependence on the radius of curvature and means of impregnation [1, 2]. In order to obtain larger spans, it is necessary to splice the timber elements on site. Feasibility studies of glulam arches with network hanger configuration have shown that it is possible to achieve timber bridges with spans in a range of 100-120 m [3, 4]. In order to maintain stability and reduce buckling problems of the timber arches, it is crucial to incorporate flexural rigidity in splice connections.

The pros and cons of different splice connection techniques in timber engineering are discussed in [5]. Recent research on self-tapping screws and long threaded rods has demonstrated the capability of these axially loaded fasteners to achieve effective connections by utilizing their high axial withdrawal capacity and stiffness. Currently, self-tapping screws and long threaded rods are mostly used as reinforcement of timber beams [6] or as connectors in a shear or axially loaded lap connections [7]. However, the performance of long threaded rods in moment resisting connections remains to be revealed. The present investigation deals with the application of long threaded rods as the main fasteners in timber splice connections subjected to bending moments. Grout-filled steel couplers (similar to systems used for reinforced pre-cast concrete) are used to connect the long threaded rods inserted in the two parts of the timber beam. The main objective of the investigation is to determine the flexural characteristics of the splice connection. Prototype splice connections were produced and investigated by full-scale experimental tests. Complementary experimental investigations were carried out to 1) identify withdrawal properties of the grouted rod splice, and 2) to establish the contact stiffness of two mutually compressed mating timber end faces. The numerical simulations performed by finite element models enabled a deeper insight into the mechanical behaviour of the tested connections. Based on the findings from both the experimental and the numerical investigations, analytical relations are proposed for determining the rotational stiffness and the moment capacity intended for practical design.

2. Problem definition

The present splice connection is intended for large glulam sections with special focus on timber network arch bridges. The dominating internal force in such structures is compression transferred by the contact of timber end faces. Shear force can be transferred via shear keys. The design philosophy is based on utilizing high withdrawal stiffness and virtually non-existing initial slip of threaded rods to achieve rotationally stiff joints that can transfer the moderate bending moments. By providing sufficient effective length, the failure mode is driven by yielding of the steel rods. This enables a more reliable prediction of the structural properties and increased ductility of the joint. Since both the threaded rods and the steel couplers are embedded in the timber, the connection is durable, fire resistant and aesthetic. Both the threaded rods and the couplers can be pre-assembled prior to transport of the timber sections; this eases the mounting process on site. It should be noted, however, that the final setting time is affected by the curing of the glue, and the gluing operation on site implies quality control issues.

The main concern regarding implementation of splice joints in glulam arches is the required rotational stiffness of the joints. The flexural characteristics of this splice connection were studied using prototype splices of timber beams. The principal layout of the prototype beam splice connection is presented in Figure 1.

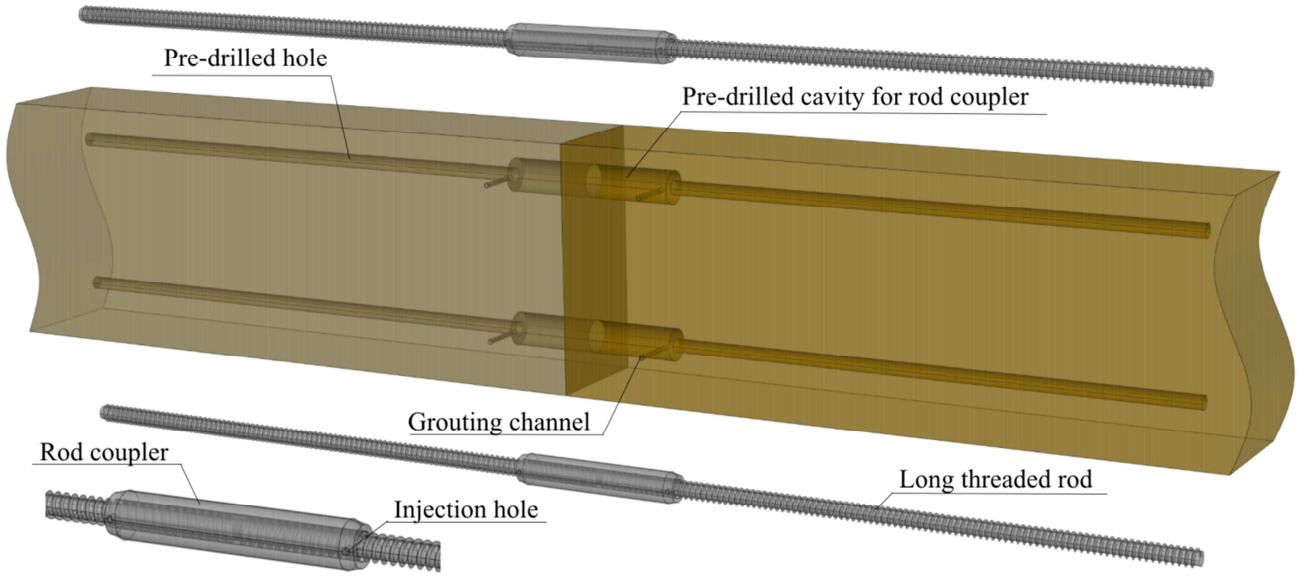

Figure 1: Principal layout of splice connection with long threaded rods and grout-filled couplers.

3. Experimental tests

3.1. Tensile test of the rod splice

Tensile testing of the rod splice was carried out in order to verify sufficient strength and to determine the withdrawal stiffness of the system of rods and grout-filled couplers. In total, 6 tensile tests were conducted. In 3 of these tests, the relative displacements of the rods were monitored by two displacement transducers (confer Figure 2). The mean value of these two measurements from each test was used to determine the deformation characteristics. Load was applied according to the loading procedure given in EN 26891:1991 [8].

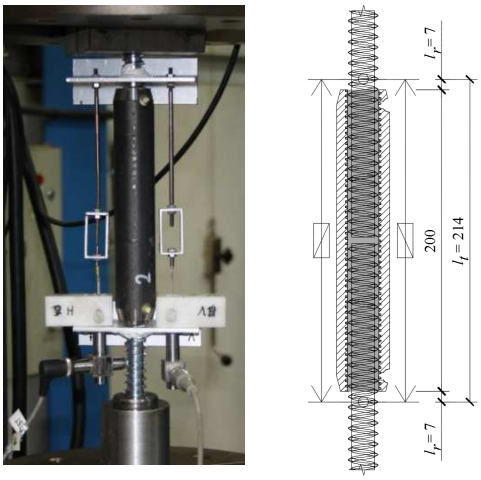

Figure 2: Test set-up of tensile test of the rod splice (dimensions given in mm).

3.2. Experimental determination of the stiffness at the interface of two mutually compressed mating timber end faces

The contact stiffness at the interface of two mutually compressed mating timber end faces was determined experimentally. The test configuration is shown in Figure 3. Two timber specimens were placed on top of each other, with direct contact of end fibers, and compressed parallel to the grain. Displacements were monitored by 8 displacement transducers. Two transducers were attached to each specimen (U and L) at two opposite faces. Four other transducers were placed at each face at the interface between the specimens. In total, 12 tests were carried out. The specimens had rectangular cross-sections of 130x130 mm^2 and the length along the grain was 300 mm. The timber specimens were sawn from glulam beams of quality GL30c [9]. The test procedure followed EN 408 [10]. More details regarding the experimental test can be found in [11].

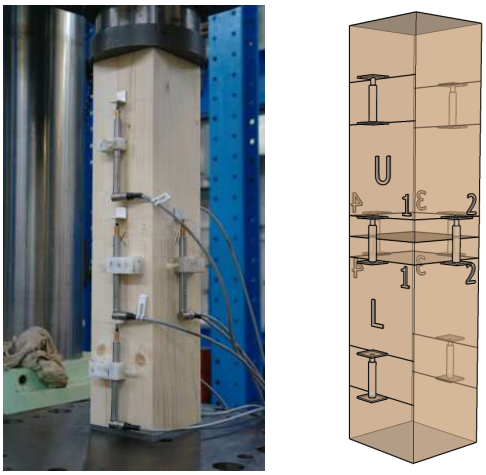

Figure 3: Test configuration for determining the stiffness at the interface of two mutually compressed mating timber end faces.

3.3. Beam splice test

The beam splice was tested in a four-point bending configuration leading to pure bending in the splice connection. The experimental set-up is shown in Figure 4. The deformation characteristics were obtained by the digital image correlation (DIC) system ARAMIS [12] and subsequent linear regression of the measured horizontal displacement field for each time step. The measurements by DIC were validated by use of additionally applied transducers. In total, two rotational transducers (denoted T1 and T2 in Figure 4) and three displacement transducers (denoted T3, T4 and T5) were placed across the end faces of the splice joint. The load was applied according to the loading procedure given in EN 26891:1991 [8].

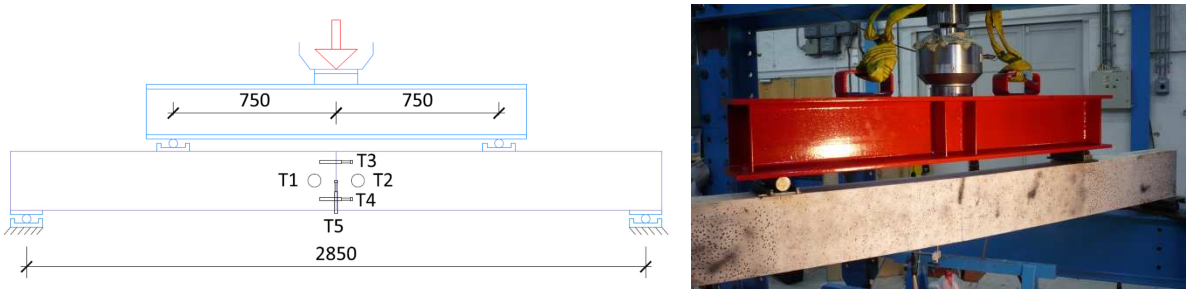

Figure 4: Experimental set-up of beam splice test (dimensions given in mm).

Four test configurations were tested, see summary in Table 1 and illustrations in Figure 5. The timber end faces of the spliced parts of the beam were placed in direct mutual contact in the configurations denoted by "C" ("C" for Contact). In the "G" configurations ("G" for Gap), the two timber parts were assembled with a 10 mm gap between the timber end faces.

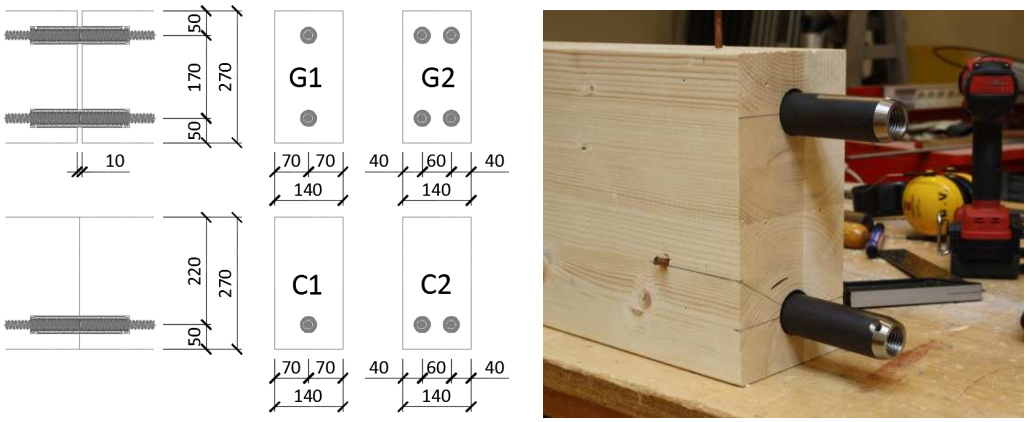

Figure 5: Test configurations of beam splice and example of production of G1 specimen (dimensions given in mm).

Table 1: Summary of the tested beam splice configurations

Config.	No. of tests	No. of rods		Timber faces
		Tension	Compression	
C1	3	1	0	Contact
C2	3	2	0	Contact
G1	3	1	1	Gap 10 mm
G2	2	2	2	Gap 10 mm

The timber beams were made of glulam strength class GL30c [9] and had 140 mm width and 270 mm depth. The beams were fabricated with 45 mm thick lamellas of Norwegian spruce. The timber specimens were conditioned at the standard environment of 20º C and 65 % relative humidity.

The threaded rods were of type SFS WB-T-20 complying with DIN 7998 [13]. The outer diameter of the rods is 20 mm, the inner diameter is 15 mm. The strength class is 8.8 according to the manufacturer. The total length of the rods was 700 mm, but the initial 100 mm was glued in the rod coupler giving an effective length of the rods equal to l_{ef} = 600 mm (the rod length screwed in timber).

The steel couplers (Figure 5 and Figure 2) were purpose made, and manufactured from steel S355. The couplers were 200 mm long with an outer diameter of 35 mm. The inner surface of the couplers was machined with metric threads M24 giving a minimum inner diameter of approximately 22 mm. Grouting, by two-component epoxy adhesive Mapei Mapepoxy L, was carried out through inserted pair of metal injection tubes, see Figure 5 (right).

4. Experimental results

4.1. Tensile test of the rod splice

All tensile tests exhibited tensile failures of the threaded rods, proving that the rod splice was stronger than the rods. Figure 6 shows the force-displacement curves of the tensile tests, carried out by the arrangement of Figure 2. The connection showed no initial slip. The mean determined axial stiffness of the rod splice, K_{co}, was 299 kN/mm (COV = 0.045). The stiffness was obtained by subtracting the deformation of the free lengths of the rods within the measured range outside the coupler (length $2l_r$ depicted in Figure 2) from the total deformation measured in the experiments (over length l_t depicted in Figure 2). Compared to the stiffness of just threaded rods of equal length, the rod splice is approximately 1.5 times stiffer. All couplers were cut open after the tests in order to visually verify the gluing efficiency. It was observed that glue filled the entire section of couplers with very low occurrence of air bubbles.

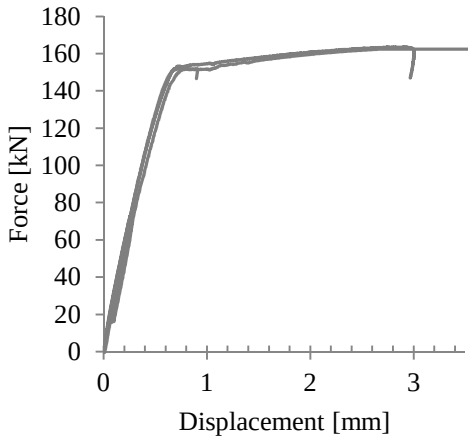

Figure 6: Force-displacement curves obtained from the tensile tests of the rod splices.

4.2. Experimental determination of the stiffness at the interface of two mutually compressed mating timber end faces

The stiffness at the interface of two mutually compressed mating timber end faces is affected by end grain effects. More details can be found in [11]. These end grain effects are described analytically by introducing a crushing zone in the vicinity of the timber end faces characterized by a crushing modulus, E_{cr}, and a crushing length, l_{cr}, schematically shown in Figure 7.

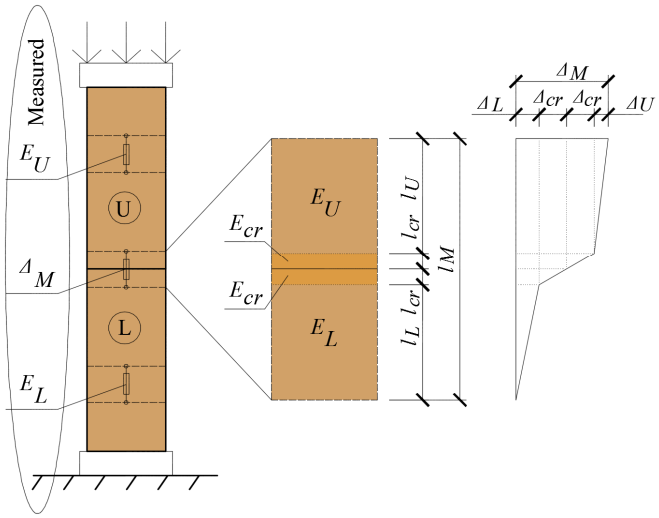

Figure 7: Schematic illustration of the analytical representation of the crushing zone characteristics.

The crushing length l_{cr} is assumed to be of equal size on both sides of the contact interface of the timber parts. With reference to Figure 7, this length is:

$$l_{cr} = \frac{1}{2} \cdot (l_M - l_U - l_L) \tag{1}$$

where l_M is the range over which the displacements Δ_M were monitored and l_U and l_L are the lengths of the upper and the lower specimen within l_M, but outside the crushing zone. Displacements monitored by displacement transducers at the interface Δ_M involve 4 contributions (after deduction of initial slip): displacements due to deformation of the upper part, Δ_U, and of the lower part, Δ_L, and two displacements due to contact at end grains Δ_{cr}. This can be expressed as:

$$\Delta_M = \Delta_U + \Delta_L + 2 \cdot \Delta_{cr} \tag{2}$$

By assuming material and dimensional homogeneity along the entire length of the test specimens and applying a relation for axially loaded strut, $\Delta = F \cdot l / (E \cdot A)$, Eq. (2) can be written as:

$$\Delta_{cr} = \frac{1}{2} \cdot (\Delta_M - \frac{F \cdot l_U}{E_U \cdot A} - \frac{F \cdot l_L}{E_L \cdot A}) \tag{3}$$

where F is the applied force corresponding to the displacements Δ_M, E_U and E_L represent the modulus of elasticity of the upper and the lower specimen, respectively, and A is the cross-sectional area of the timber specimens.

The stiffness of the crushing zone is finally expressed by the crushing modulus E_{cr} and the crushing length l_{cr} as:

$$\frac{E_{cr}}{l_{cr}} = \frac{F}{A \cdot \Delta_{cr}} \tag{4}$$

The mean values of the experimental results (COV = 0.225) are presented in Figure 8 for an extent of the crushing length up to 3 mm, which is considered to be the upper limit, based on observations during testing. The experimental results show that the crushing stiffness is much lower than the material stiffness. However, the extent of the crushing zone is very limited, of the order of 1 mm, as observed visually and identified from the measurements by displacement transducers. The deformation of the crushing zone during and after testing is illustrated in Figure 9.

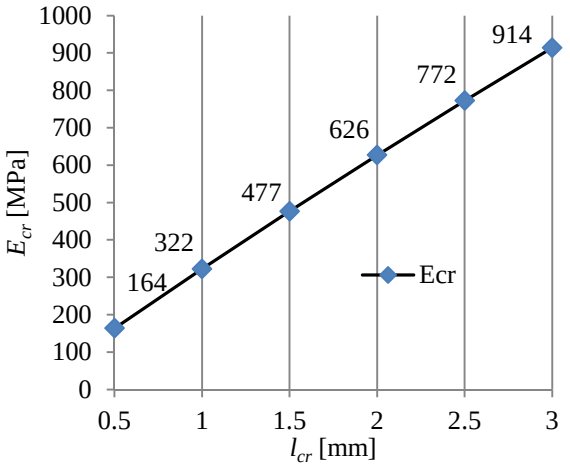

Figure 8: Experimentally determined stiffness at the interface of two mating timber end faces.

By comparing the stiffness of the crushing zone E_{cr} / l_{cr} given in Figure 8, it can be noticed that the stiffness is not significantly affected by the extent of the crushing zone. For practical use, it is thus suggested to use l_{cr} = 3 mm with the corresponding E_{cr} = 914 MPa, yielding the stiffness of the crushing zone $E_{cr} / l_{cr} \cong 300\ \mathrm{N / mm^3}$.

Figure 9: Deformation of the crushing zone during testing (left), and deformation pattern at the end faces after testing (right).

4.3. Beam splice test

Table 2: Experimental results of bending tests of splice connection

Config. Mean	No.of tests	M_u			k_θ			a_0	
		[kNm]	COV	η_M [(a)]	[kNm/rad]	COV	η_k [(b)]	[mm]	COV
G1	3	19.1	0.05	27 %	1826	0.08	48 %	105	0.16
G2	2	43.6	0.02	62 %	4016	0.02	67 %	100	0.06
C1	3	25.6	0.14	36 %	2093	0.08	52 %	112	0.05
C2	3	48.1	0.04	69 %	3749	0.07	66 %	143	0.12

input: GL30c: [(a)] $f_{m,m}$=41.4 MPa [(b)] E=13000 MPa, G=650 MPa

Experimental results of bending tests of the splice connections are given in terms of moment vs. rotation in the joint, see the plots in Figure 10. The ultimate moment M_u, the elastic rotational stiffness k_θ and the distance of neutral axis from the upper timber edge a_0 (illustrated in Figure 14) are presented in Table 2. The splice efficiency with respect to moment capacity, η_M, is the ratio between the measured ultimate moment and the mean bending capacity of the unspliced timber cross-section. The efficiency with respect to rotational stiffness, η_k, relates the mid-span deflection of an unspliced beam to that of a beam containing a splice connection (the respective deflections were obtained analytically by the principle of virtual work).

All specimens failed due to withdrawal of the tension rods, see the detail at the rod-end in Figure 11b. The C2 configuration was characterized by brittle failure occurring shortly after the ultimate capacity had been reached (see Figure 10). This may indicate a risk of progressive failure of the group of rods caused by low ductility of withdrawal failure of rods parallel to the grain [14]. A crack parallel to the grain and close to the neutral axis occurred for two C2

specimens, see Figure 11a. This crack is most likely induced by tensile stresses perpendicular to the grain caused by a change of slope at the rotated end faces.

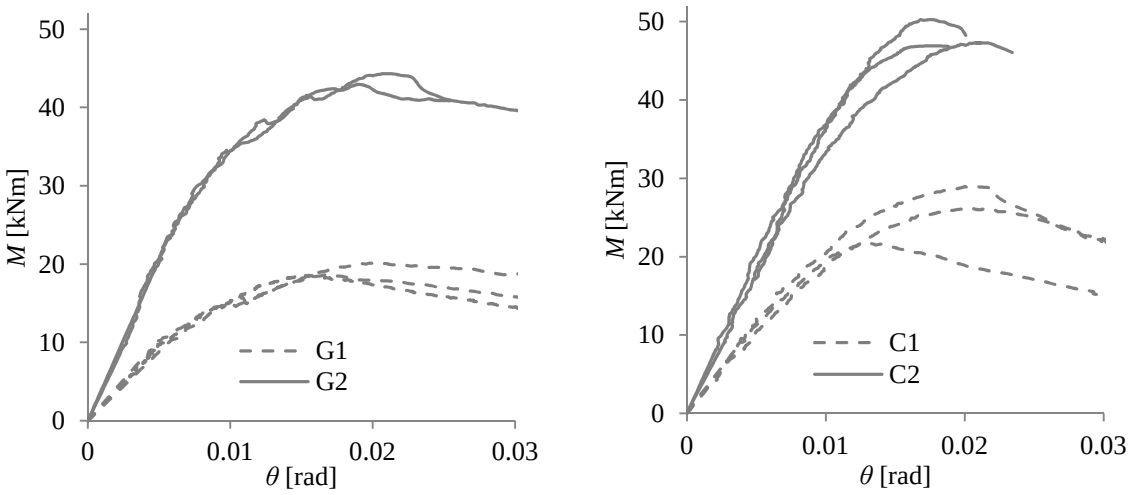

Figure 10: Moment-rotation curves based on data from DIC monitored during bending tests.

The curves plotted in Figure 10 are limited either by a rotation of 0.03 rad or by specimen failure. The relative rotations θ were obtained by linear regression of horizontal displacements, monitored by DIC along the entire length of the vertical sections (i.e. considering both deformations above and under the neutral axis) placed in the vicinity of the timber end faces. The values obtained by linear regression of DIC results were in good agreement with the rotations measured by the rotational transducers. Common for all tests: no initial slip was observed, facilitating an immediate load take-up in the joint. This is an important prerequisite for the moment resisting connections, especially in statically indeterminate structures, for which an additional deformation in the joint causes a redistribution of internal forces within the structure [15].

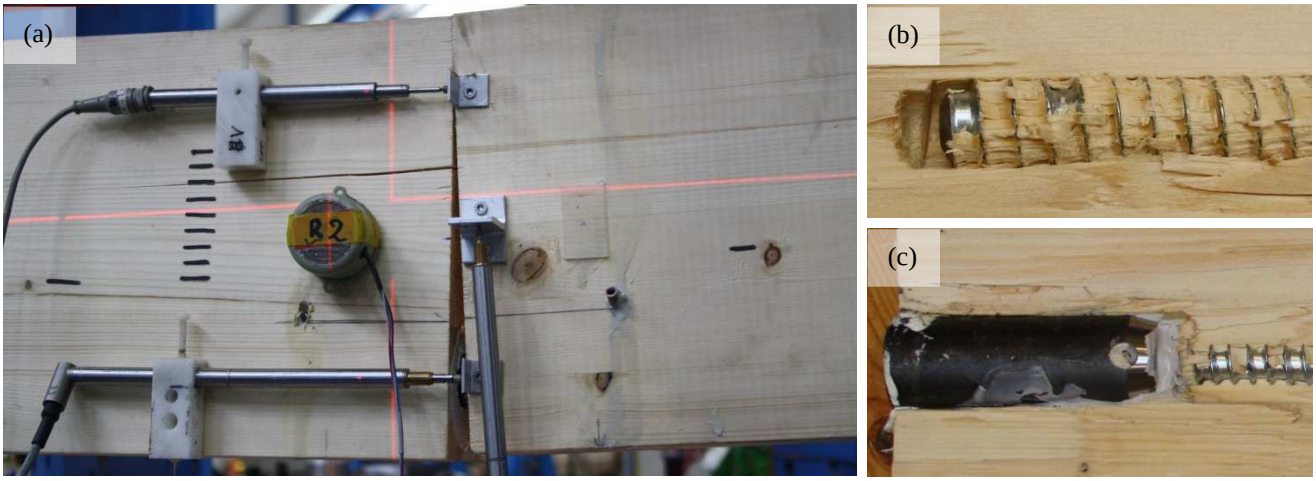

Figure 11: Detail of a C2 specimen during testing (a), Cut-opened specimens after testing: Withdrawal failure of a tension rod (b), a compression coupler with the cavity in timber filled with glue (c).

The relative moment capacities and rotational stiffnesses for configurations with two rods as compared to one rod show no obvious signs of a group effect in case of two rods (which suggests $n_{ef} = n$ with reference to EC5 [16] 8.7.2).

Some additional parameters obtained from the analysis of the bending test results in conjunction with the proposed analytical model, are summarized in Table 3.

Table 3: Ultimate tensile force in rod F_{tu}, withdrawal stiffness of rod K_w, and crushing modulus E_{cr} obtained by analysis of beam splice test results

All conf.	F_{tu}		K_w		E_{cr} [(a)]	
	[kN]	COV	[kN/mm]	COV	[MPa]	COV
Mean	128	0.11	264	0.10	114	0.24

[(a)] for C-configuration and assuming l_{cr} = 3 mm

It is interesting to notice that the withdrawal stiffness K_w obtained here, is considerably larger than the value obtained by withdrawal tests reported by Stamatopoulos et al. [14]. The latter was obtained from pure axial withdrawal of threaded rods in pull-push test configuration.

The crushing modulus E_{cr}, obtained from the bending tests, is much smaller than the value obtained from the separate tests, as described in Section 4.2. While the tests of end grain effects yield a uniform stress distribution in the compressed area, the bending tests produce a varying stress distribution in the compression zone. Another factor is uncertainty in the fabrication process of the splice connections. The joints were not pre-compressed during hardening of the glue in the rod couplers, and the planeness of the end surfaces was in general lower for the specimens of the bending tests. Consequently, the end faces may have had non-uniform contact.

5. Numerical model of beam splice tests

Numerical simulations of the beam splice were carried out by ABAQUS [17]. Each geometrical configuration tested in the experiments was modelled by eight-node brick elements with reduced integration and hour-glass control (C3D8R). Given the symmetry of the problem, only half the beam was modelled, see Figure 12. Transverse displacements of the beam were prevented. Loading was applied by normal pressure at the top of the beam, corresponding to 4-point bending as shown in Figure 4.

The contact stiffness between the end timber faces at the splice joint was modelled by implementing the "crushing zone" in the vicinity of the joint. The experimental values from the bending tests were used as an input to the numerical model (l_{cr} = 3 mm and E_{cr} = 114 MPa, see Table 3 and further discussion in Section 7.2).

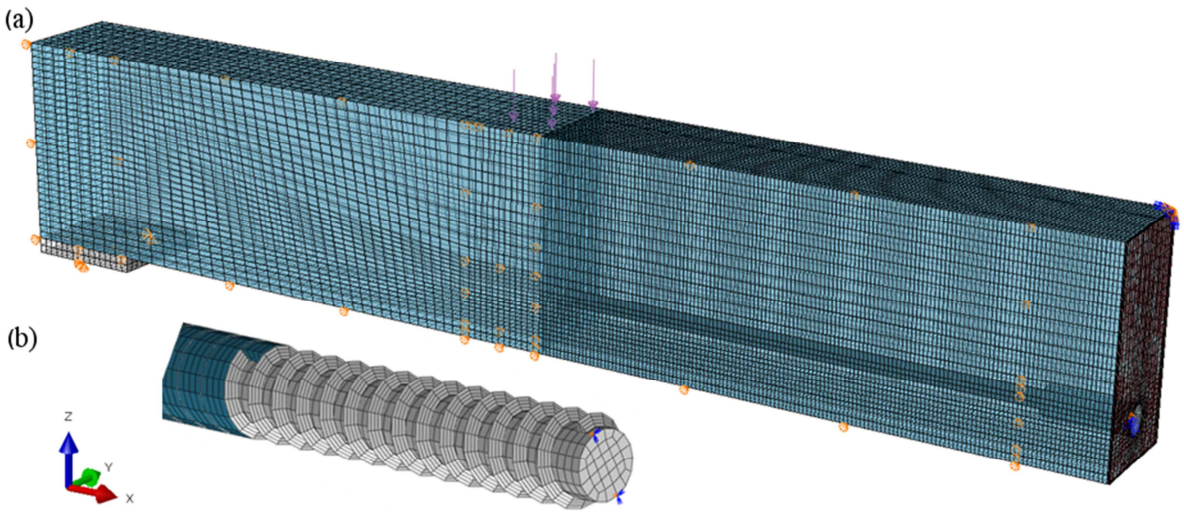

Figure 12: Finite element model for C1 configuration (a) and detail of threaded rod with female part of surrounding timber (b).

The rods and their interaction with the timber were based on a numerical model presented in [14]. Contact properties between rod and timber utilize a "hard" contact behaviour in the normal direction and isotropic tangential behaviour with a coefficient of friction of 0.2. The rod couplers were not included in the numerical model. The axial stiffness of the rod splice in the coupler was accounted for by converting the experimentally obtained stiffness (K_{co} = 299 kN/mm, see Section 4.1) into an equivalent modulus of elasticity (338 GPa), applied to the initial 100 mm portion of the rod core (see Figure 12b).

Material properties of wood were assumed to be transversely isotropic, see Table 4. Here, E is modulus of elasticity, G is shear modulus and v is Poisson's ratio. The longitudinal direction (L) is the grain direction, and no distinction is made between tangential (T) and radial (R) directions. Steel was modelled as isotropic with E = 210 GPa and v = 0.3.

Table 4: Material properties of wood used in numerical simulations

E_L [MPa] [a]	E_R=E_T [MPa] [a]	G_{LR}=G_{LT} [MPa] [b]	G_{RT} [MPa] [b]	v_{LR}=v_{LT} [-] [b]	v_{TR} [-] [b]
13000	400	600	30	0.6	0.315

[a] Manufacturer: Moelven industrier ASA, class L40 (GL30c)

[b] Norwegian spruce [18]

6. Analytical model

Tests of timber splice connections using glued-in hardwood dowels [19] and glued-in rods [20, 21] demonstrated the importance of incorporating the slip of connectors when predicting the height of the compression zone and the rotational stiffness. Moreover, it was observed in [20] that the stiffness of timber in compression is affected by deformation at end grains of the timber end faces. The present analytical model accounts for both slip of connectors and for deformation at end grains.

6.1. Prediction of rotational stiffness

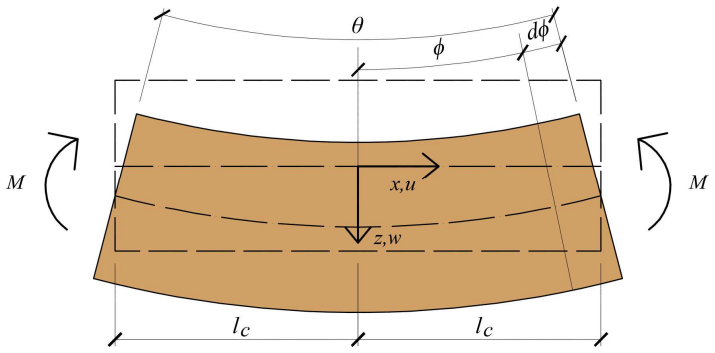

Figure 13: Beam portion subjected to a bending moment.

Figure 13 shows the deformed state of a portion of a beam of length $2l_c$ subjected to a bending moment M. The bending moment produces a relative rotation θ at the end sections of the beam portion. By assuming small deformations and rotations, and Navier's hypothesis of plane sections remaining plane during deformation, the following relations of the Euler-Bernoulli beam theory apply:

$$\phi \approx \tan\phi = -\frac{dw}{dx}$$
$$\kappa = \frac{d\phi}{dx} = -\frac{d^2 w}{dx^2} \tag{5}$$
$$\varepsilon_x = z \cdot \frac{d\phi}{dx} = z \cdot \kappa$$

The slope ϕ is also the rotation of the beam section (Navier), κ is the curvature of the deformed beam and ε_x is the longitudinal strain. Using (5), the relative rotation of the end sections of the beam portion is found to be:

$$\theta = \int_{-l_c}^{l_c} \frac{d\phi}{dx} dx = 2 \cdot \kappa \cdot l_c \tag{6}$$

Solving Eq. (6) with respect to κ and inserting the result into the expression for ε_x in (5), Hooke's law gives:

$$\sigma_x = E \cdot \varepsilon_x = E \cdot z \cdot \frac{\theta}{2 \cdot l_c} \tag{7}$$

where σ_x is normal axial stress and E is modulus of elasticity parallel to the grain.

The analytical model is based on Eq. (6). Figure 14 shows a deformed splice connection with a relative rotation θ of the end faces caused by the bending moment M. Here, h and b are height and width of cross-section respectively, a_0 is the height of wood in compression, a_i is a coordinate along z-axis of i-th row of the rods determined from the upper edge of wood in compression, l_c represents equivalent length of compression zone at each side of the connection, σ_x is normal stress in wood, K_{si} is axial stiffness of the i-th row of the rods, u_i is horizontal displacement at the i-th row of the rods and $z_i = a_i - a_0$ is the z-coordinate of the the i-th row of steel rods.

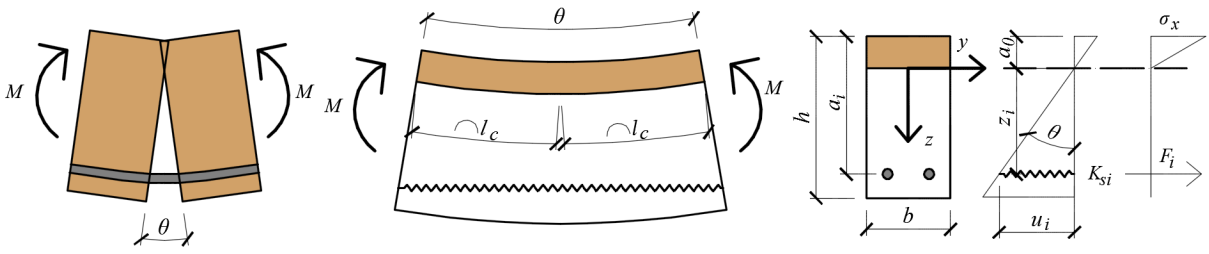

Figure 14: Analytical model characteristics.

The relative rotation of the end faces of the splice connection is approximated by a relative rotation of the end sections of a beam portion of length $2l_c$. The flexural stiffness is thus governed by the deformation of the wooden part in compression and the elongation of a spring representing the axial stiffness of the steel rods.

The axial force in the i-th row of steel rods is found by:

$$F_i = K_{si} \cdot u_i = K_{si} \cdot \theta \cdot z_i \tag{8}$$

The horizontal force equilibrium reads:

$$\sum_{i=1}^{n} F_i - \int_{0}^{-a_0} \int_{-\frac{b}{2}}^{\frac{b}{2}} \sigma_x dy dz = 0 \tag{9}$$

Using Eq. (7) and Eq. (8), Eq. (9) takes the following form:

$$\sum_{i=1}^{n} K_{si} \cdot (a_i - a_0) - \frac{E \cdot b \cdot a_0^2}{4 \cdot l_c} = 0 \tag{10}$$

Finally, the height of wood in compression is obtained by solving Eq. (10) for a_0. The equation yields two roots, only one of which is physically possible:

$$a_0 = \frac{-\sum_{i=1}^{n} K_{si} + \sqrt{\left(\sum_{i=1}^{n} K_{si}\right)^2 + \frac{E \cdot b}{l_c} \cdot \sum_{i=1}^{n} K_{si} \cdot a_i}}{\frac{E \cdot b}{2 \cdot l_c}} \tag{11}$$

The moment at the connection about the y-axis is:

$$M = \sum_{i=1}^{n} F_i \cdot z_i - \int_{0}^{-a_0} \int_{-\frac{b}{2}}^{\frac{b}{2}} \sigma_x \cdot z dy dz \tag{12}$$

Using Eq. (7) and Eq. (8), Eq. (12) takes the following form:

$$M = \theta \cdot \left(\sum_{i=1}^{n} K_{si} \cdot z_i^2 + \frac{E \cdot b \cdot a_0^3}{6 \cdot l_c} \right) \tag{13}$$

The rotational stiffness of the connection k_θ is then obtained as:

$$k_\theta = \frac{M}{\theta} = \sum_{i=1}^{n} K_{si} \cdot z_i^2 + \frac{E \cdot b \cdot a_0^3}{6 \cdot l_c} \tag{14}$$

The axial stiffness of the i-th row of steel rods, K_{si}, is given by Eq. (15) and it is obtained as an effective stiffness of a system of three springs representing the axial withdrawal stiffnesses of the threaded rods at each side of the connection,

denoted as K_w, and the axial stiffness of the joint of threaded rods in the rod coupler, denoted as K_{co}. The number of steel rods in one row is denoted as n_r.

$$K_{si} = n_r \cdot \frac{K_w \cdot K_{co}}{2 \cdot K_{co} + K_w} \tag{15}$$

The equivalent length of compression zone, l_c , consists of two contributions as shown in Figure 15, and is given by the following equation:

$$l_c = l_0 + l_{cr} \cdot \frac{E}{E_{cr}} \tag{16}$$

where l_0 is the effective length of the compression zone, and E_{cr} and l_{cr} are the crushing modulus and the crushing length, respectively.

The effective length of the compression zone, l_0, characterizes the compliance of the wood in compression. This length approximately defines a local area, in close proximity to the splice joint, for which the Navier's hypothesis is violated and where the stress state is a combination of compression stresses parallel to the grain, tensile stresses perpendicular to the grain and shear stresses.

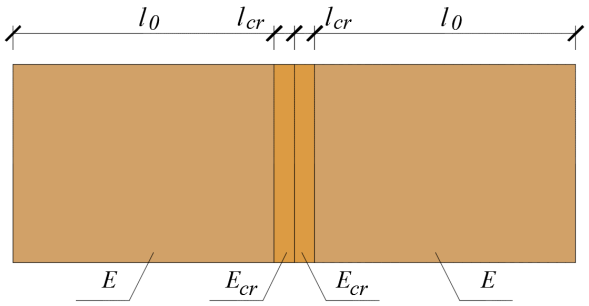

Figure 15: Graphical representation of the equivalent length of the compression zone.

It is proposed to estimate l_0 as a simple function of the height of the timber cross-section h:

$$l_0 = 0.85 \cdot h \tag{17}$$

This relation was obtained based on investigations using numerical models. Given validity of the form of Hooke's law and Navier's hypothesis adopted for the model, the length l_0 within the compression zone reads $l_0 = E \cdot u / \sigma_x$. The extent of the horizontal displacements u is a function of the height of the cross-section h, elastic moduli parallel (E_0) and perpendicular (E_{90}) to the grain, and shear modulus G. A parametric numerical study showed that l_0 is constant for constant relations between E_0, E_{90}, and G, which is the case for structural timber ($G = E_0 / 16$, $E_{90} = E_0 / 30$ in [22]) and

which can also be assumed to be valid for glulam. The suggested length l_0 in Eq. (17) is thus independent of the timber strength class.

The deformation at the end grains of two mutually compressed mating timber end faces is described by the second contribution in Eq. (16). It is derived by introducing a crushing zone characterized by a crushing modulus, E_{cr}, and a crushing length, l_{cr}. The parameters of the crushing zone were obtained experimentally. A comparison of the horizontal displacements at the splice joint, obtained by numerical models, with and without a crushing zone, is demonstrated in Figure 16 (left). An example of the horizontal displacements over the beam height at the splice joint, obtained by DIC during one of the bending tests, is shown to the right in Figure 16. Figure 16 demonstrates good agreement between the numerical model with the crushing zone (blue line) and measurement by DIC.

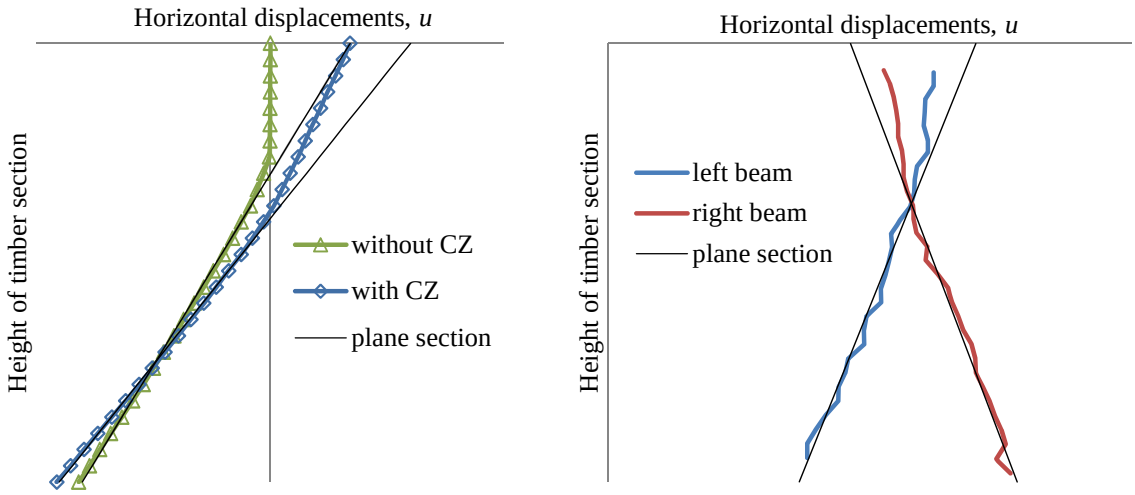

Figure 16: Horizontal displacements along vertical sections at beam joint: Left: Output from numerical models with and without crushing zone (CZ), Right: Example of results obtained by DIC during one of the bending tests.

The determination of the position of the neutral axis and the rotational stiffness in the configuration with no contact of timber end faces is carried out by use of Eq. (10) and Eq. (14), respectively, with omitting the terms associated with the compression stresses in the timber.

6.2. Prediction of moment capacity

For one single row of threaded rods in the tension side, or one in the tension and one in the compression side, the moment capacity is obtained from simple moment equilibrium of compression and tension force acting at the joint:

$$M_u = \min(F_{tu}; F_{cu}) \cdot z_c \tag{18}$$

where F_{tu} and F_{cu} are the ultimate strengths of components in tension and compression obtained by Eq. (19), and z_c is the lever arm of the internal forces. With reference to Figure 14, z_c is determined by assuming that F_{cu} acts at $a_0 / 3$.

$$F_{tu} = n_r \cdot \min(R_{axu}; R_u)$$
$$F_{cu} = \frac{1}{2} \cdot b \cdot a_0 \cdot f_{c,0} \tag{19}$$

Here, $f_{c,0}$ is the timber strength in compression parallel to the grain, R_u is the tensile strength of the rods (provided by the manufacturer) and R_{axu} is the ultimate withdrawal strength of threaded rods.

6.3. Ultimate withdrawal strength of threaded rods

The withdrawal strength of threaded rods R_{ax} was determined by Stamatopoulos et al. [23]. However, in this particular connection, the rods are loaded by a combination of axial withdrawal force and local bending moment induced by the rotational restraint at the point where the rod enters the coupler. Hence, the ultimate withdrawal strength of the rods, R_{axu}, is less than that of rods in pure tension, R_{ax}. Since the withdrawal strength of threaded rods is (approximately) a linear function of the effective length [23], the ultimate withdrawal strength is determined on the basis of a reduced effective length of the threaded rods:

$$R_{axu} = R_{ax} \cdot \left(\frac{l_{ef} - l_x}{l_{ef}} \right) \tag{20}$$

The effective length of the threaded rods (length of the rod screwed in timber) is denoted l_{ef}, whereas l_x is a free length of rod that is not considered to contribute to the withdrawal capacity. This free length is estimated as follows. In the same way as the models developed for connections with fully threaded self-tapping screws [24], the threaded rod is considered as a semi-infinite beam on elastic foundation loaded by a bending moment M_0, see Figure 17.

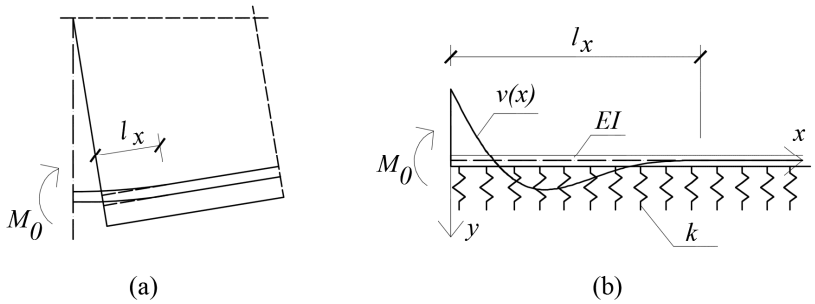

Figure 17: Simplified illustration (rod couplers are not included) of an imposed local bending moment at the end of the rod (a), analogy with semi-infinite beam on elastic foundation (b).

The differential equation for the deflection curve of a beam supported on an elastic foundation is:

$$EI\frac{d^4y}{dx^4} = -k \cdot y \tag{21}$$

where k is the foundation stiffness (N/mm^2) and EI represents the flexural stiffness of the beam. By introducing the characteristic length λ and solving the differential equation with boundary conditions corresponding to the arrangement shown in Figure 17b, the deflection curve becomes [25]:

$$y = \frac{2M_0 \cdot \lambda^2}{k} e^{-\lambda \cdot x}(\cos(\lambda \cdot x) - \sin(\lambda \cdot x)) \;;\; \lambda = \sqrt[4]{\frac{k}{4EI}} \tag{22}$$

The length l_x is found by solving Eq.(22) with respect to x for $y = 0$, and considering the second period, see Figure 17b:

$$l_x = \frac{5\pi}{4\lambda} = \frac{5}{8}\pi \cdot d_c \cdot \sqrt[4]{\frac{\pi \cdot E_s}{k_t}} \tag{23}$$

where d_c is the core diameter of the threaded rods, E_s is the elastic modulus of steel and k_t is the foundation modulus of timber transverse to the grain.

7. Model evaluation compared to experimental results

Table 6 presents an overview of experimentally, analytically and numerically obtained parameters. The input parameters to the analytical model are summarized in Table 5. For the nomenclature of the input parameters, see Section 6.

Table 5: Input parameters to the analytical model

K_w [kN/mm]	K_{co} [kN/mm]	E [MPa]	E_{cr} [MPa]	l_{cr} [mm]	R_{ax} [kN]	k_t [MPa]
264	299	13000	114	3	161	710
Table 3	Sect. 4.1	Table 2	Table 3	Table 3	[23] [(a)]	[26, 27] [(b)]

[(a)] Mean value from experimental investigation

[(b)] Average of experimental results for spruce and steel dowels of diameter 16 mm (763 MPa [26] and 658 MPa [27])

Table 6: Result comparison for ultimate moment M_u, rotational stiffness k_θ, and distance of neutral axis from the upper timber edge a_0

Config. Mean	M_u [kNm]		k_θ [kNm/rad]			a_0 [mm]		
	Exp.	Anal.	Exp.	Anal.	Num.	Exp.	Anal.	Num.
G1	19.1	20.2	1826	1818	1294	105	103	132
G2	43.6	40.3	4016	3636	2762	100	103	132
C1	25.6	21.7	2093	1787	2126	112	113	108
C2	48.1	41.4	3749	2577	3458	139	136	137

7.1. Analytical model comparison to experimental results

The analytical model gives, in general, good estimates of both the rotational stiffness and the moment capacity, see Table 6. The predicted rotational stiffness for the C configurations is conservative due to the assumed planeness of end timber sections (Navier). However, the Navier's hypothesis is, in fact, violated in close proximity to the end timber faces, as shown in Figure 16. In the experiments, the reduced horizontal displacements within the compression zone result in a lower monitored rotation and thus a higher rotational stiffness.

The prediction of moment capacity for the C configurations, with the neutral axis determined by the assumed elastic behaviour by Eq. (11), is somewhat conservative. Conferring Table 6, the predicted capacities are approximately 15 % lower, compared to experimental results. As the tensile forces in the rods approach the ultimate withdrawal strength, the withdrawal stiffness of the rods gradually decreases [14, 23]. The neutral axis thus gradually moves towards the upper edge of the timber cross-section and the lever arm of the internal forces increases. However, the increasing rotation in the joint gives rise to shear stresses and tensile stresses perpendicular to the grain in the compression zone, due to change of slope at the rotated end faces, as shown in Figure 16. It was observed in the experiments that the possible "plastification"

of the compression zone is accompanied by occurrence of cracks along the grain near the neutral axis, see Figure 11a. If no measures are taken to reinforce the timber perpendicular to the grain, it is most appropriate to predict the moment capacity based on the elastic behaviour assumption.

The crushing modulus E_{cr} based on the experimental results obtained from the bending tests was used as an input parameter to the analytical model. The use of crushing modulus obtained from the uniaxial tests of end grain effects provided overly stiff predictions, compared to the results from the bending tests.

From the cut-outs of the specimens after tests, it was observed that voids in the timber around the steel couplers were well filled with glue (see Figure 11c), which allowed a force transfer between the couplers and the timber at the compression side. Consequently, the axial stiffness K_{si} at the compression side, monitored in experiments, was 2.2 times higher than the stiffness at the tension side. This was taken into account in the neutral axis prediction by the analytical model. The "pushing-in" stiffness of long threaded rods was studied using numerical models. This stiffness was found to be 1.1 times higher than the withdrawal stiffness, K_w, of the rods.

7.2. Numerical model comparison to experimental results

The numerical model predicts the rotational stiffness for the C configurations with good accuracy, while the rotational stiffness for the G configurations is underestimated by approximately 25 %, confer Table 6. The distance of the neutral axis from the upper timber edge a_0, obtained by the numerical models for the G configurations, is somewhat larger than obtained experimentally. These discrepancies are caused by the fact that the numerical model does not account for the contact forces between the rod couplers and the timber. A possible future improvement of the model can be facilitated by physically modelling the steel couplers and defining contact surfaces between the rods and the couplers, and between the couplers and the timber.

The mean withdrawal stiffness obtained by the numerical analyses was 258 kN/mm, which is in good agreement with the experimentally obtained value.

Similar to the analytical model, E_{cr} obtained from the bending tests was used as an input to the numerical models. The use of the crushing modulus obtained from the uniaxial tests of end grain effects yielded an excessively stiff model, compared to the results from the bending tests.

8. Concluding remarks

The investigation revealed that high moment capacity and rotational stiffness of timber splice connection can be achieved by application of long threaded rods. The tested connection showed no initial slip, which is an important pre-requisite for an application in moment-resisting connections. A rather brittle failure, caused by withdrawal of the threaded rods, was encountered for all experimental tests of the splice connection. The ductility was, however, much higher than for unspliced timber beams. Both ductility and capacity of the connection can be enhanced by yielding in rods, achieved by use of larger effective length of the rods.

Capacity and withdrawal stiffness of the rod splice, by grout-filled couplers, were sufficient and reliable. None of the experimental tests failed at the joint of the rods. The grouting process was straightforward and easy to implement.

The finite element model simulates effectively flexural behaviour of the joint. Application of a crushing zone at the joint allows for modelling of end grain effects of two mutually compressed timber end faces.

The proposed analytical models yield slightly conservative estimates of both the rotational stiffness and the moment capacity of the splice connection. Input parameters to these models are proposed based on the numerical analyses and the experimental tests.

The orientation of the threaded rods in the grain direction enables direct force transfer in the axial direction. It also utilizes the high withdrawal stiffness of rods parallel to the grain. On the other hand, since withdrawal of the rods is characterized by brittleness, it can lead to progressive failure of a group of rods. Furthermore, the development of shrinkage cracks (in the grain direction) in close proximity to the threaded rods can lead to loss of capacity. These shortcomings can be overcome by using long threaded rods with a small inclination to the grain. Further investigations are, however, necessary to examine for instance the effect of an implied lateral force component at the end of the rods.

Acknowledgment

This work was funded by the WoodWisdom-Net+ project DuraTB (“Durable Timber Bridges”) and the support from the funding bodies and partners is gratefully acknowledged. The authors would also like to acknowledge Mathias Strøm and Christoffer Aune Moe for their important contributions and experimental work.

References

[1] T. Dyken, Trebruer - Statens Vegvesens rapport Nr.422 (Timber bridges - Norwegian Public Roads Administration report Number 422), Statens Vegvesen (Norwegian Public Roads Administration), 2017.

[2] F. Colling, Glued laminated timber - Production and strength classes, Timber Engineering STEP 1, 1995.

[3] K. Bell, Structural systems for glulam arch bridges, International Conference on Timber Bridges (ICTB 2010), Lillehammer, Norway, 2010.

[4] K.A. Malo, A. Ostrycharczyk, R. Barli, I. Hakvåg, On development of network arch bridges in timber, International Conference on Timber Bridges (ICTB 2013), Las Vegas, USA, 2013.

[5] M. Cepelka, K.A. Malo, Review on on-site splice joints in timber engineering, COST-Timber Bridges Conference 2014, Biel/Bienne, 2014.

[6] P. Dietsch, R. Brandner, Self-tapping screws and threaded rods as reinforcement for structural timber elements – A state-of-the-art report, Construction and Building Materials 97 (2015) 78-89.

[7] R. Tomasi, A. Crosatti, M. Piazza, Theoretical and experimental analysis of timber-to-timber joints connected with inclined screws, Construction and Building Materials 24(9) (2010) 1560-1571.

[8] CEN, EN 26891:1991 (ISO 6891:1983) Timber structures, Joints made with mechanical fasteners, General principles for the determination of strength and deformation characteristics 1991.

[9] CEN, EN 14080:2013: Timber structures-Glued laminated timber and glued solid timber - Requirements, European Committee for Standardization, 2013.

[10] CEN, EN 408:2010+A1:2012: Timber structures - Structural timber and glued laminated timber - Determination of some physical and mechanical properties, European Committee for Standardization, 2012.

[11] M. Cepelka, K.A. Malo, Experimental study of end grain effects in timber joints under uniaxial compression load, in: W.W. J. Eberhardsteiner, A. Fadai, M. Pöll (Ed.) Proceedings of the World Conference on Timber Engineering (WCTE 2016), August 22-25, 2016, Vienna University of Technology, Austria, ISBN: 978-3-903039-00-1, Vienna, Austria, 2016.

[12] GOM Optical Measuring Techniques, ARAMIS, User Manual-Software, 2009.

[13] DIN, DIN 7998: Gewinde und Schraubenenden für Holzschrauben (Threads and screws for wood), Deutsches Institut für Normung, Berlin, 1975.

[14] H. Stamatopoulos, K.A. Malo, Withdrawal stiffness of threaded rods embedded in timber elements, Construction and Building Materials 116 (2016) 263-272.

[15] A.J.M. Leijten, Requirements for moment connections in statically indeterminate timber structures, Engineering Structures 33(11) (2011) 3027-3032.

[16] CEN, EN 1995-1-1:2004: Design of timber structures. Part 1-1: General-Common rules and rules for buildings, European committee for standarization, Brussels, 2004.

[17] D.S.S.C. DSS, Abaqus analysis user's guide, Version 6.14, 2014.

[18] K.B. Dahl, Mechanical properties of clear wood from Norway spruce. Dissertation, Department of Structural Engineering, Norwegian University of Science and Technology, 2009.

[19] T. Sasaki, A. Koizumi, J.L. Jensen, Y. Iijima, Y. Tamura, K. Komatsu, End joint with glued-in hardwood dowels in timber construction I. Bending properties of beams jointed with single row of dowels, Mokuzai Gakkaishi/Journal of the Japan Wood Research Society 45(1) (1999) 17-24.

[20] J.L. Jensen, P. Quenneville, Connections with glued-in rods subjected to combined bending and shear actions, CIB-W18/42-7-9 International council for research and innovation in building and construction working commission W18 - Timber structures, 2009.

[21] B.H. Xu, A. Bouchaïr, P. Racher, Analytical study and finite element modelling of timber connections with glued-in rods in bending, Construction and Building Materials 34 (2012) 337-345.

[22] CEN, EN 338:2009: Structural timber - Strength classes, European Committee for Standardization, 2009.

[23] H. Stamatopoulos, K.A. Malo, Withdrawal capacity of threaded rods embedded in timber elements, Construction and Building Materials 94 (2015) 387-397.

[24] F. Moshiri, R. Shrestha, K. Crews, The Predictive Model for Stiffness of Inclined Screws as Shear Connection in Timber-Concrete Composite Floor, RILEM Bookseries, 2014, pp. 443-453.

[25] M. Hetényi, Beams on elastic foundation: Theory with applications in the fields of civil and mechanical engineering, The University of Michigan Press, Baltimore, 1946.

[26] N. Gattesco, Strength and local deformability of wood beneath bolted connectors, Journal of Structural Engineering 124(2) (1998) 195-202.

[27] N. Gattesco, I. Toffolo, Experimental study on multiple-bolt steel-to-timber tension joints, Materials and Structures/Materiaux et Constructions 37(266) (2004) 129-138.